



ELSEVIER

Contents lists available at ScienceDirect

## Surface &amp; Coatings Technology

journal homepage: [www.elsevier.com/locate/surfcoat](http://www.elsevier.com/locate/surfcoat)

## Laser coating of a Zr-based metallic glass on an aluminum substrate

Navid Sohrabi<sup>a,\*</sup>, Ramanandan Santhanu Panikar<sup>a</sup>, Jamasp Jhabvala<sup>a</sup>, Alejandro Roda Buch<sup>b</sup>, Stefano Mischler<sup>b</sup>, Roland E. Logé<sup>a</sup><sup>a</sup> Thermomechanical Metallurgy Laboratory, PX Group Chair, Ecole Polytechnique Fédérale de Lausanne (EPFL), CH-2002 Neuchâtel, Switzerland<sup>b</sup> Tribology and Interface Chemistry Group, Ecole Polytechnique Fédérale de Lausanne (EPFL), CH-1015 Lausanne, Switzerland

## ARTICLE INFO

## Keywords:

Additive manufacturing  
Metallic glasses  
Crystallization  
Laser processing  
Aluminum alloy  
Cladding

## ABSTRACT

Cladding of a Zr-based metallic glass (MG) on an aluminum substrate was conducted using a layer-wise laser additive manufacturing (AM) method, leading to relative densities higher than 99%. The thickness of the cladding was about 300  $\mu\text{m}$ . The effect of laser power on the bonding with the substrate was investigated. Laser parameters changed from the interface to the bulk of the cladding, such as to obtain both a highly amorphous coating, and excellent bonding with the substrate. The coating microstructures and properties were analyzed in terms of crystallized fraction and micro-hardness. The wear resistance of the cladding was 20 times better than that of the substrate.

## 1. Introduction

Aluminum and their alloys are of great attraction for aerospace, automotive, and sport equipment applications because of their light-weight, high strength to weight ratio, and corrosion resistance properties. Unfortunately, low wear resistance and hardness have limited their applications [1,2].

Metallic Glasses (MGs) refer to metallic alloys that do not have a long-range order in their atomic structure, i.e., they are amorphous [3]. In practice, MGs are produced by cooling the melt quickly enough such that the atoms cannot arrange into the ordered configuration inherent to conventional crystalline materials [4]. Due to the non-conventional atomic arrangement, MGs possess enhanced properties such as excellent hardness and strength, magnificent corrosion and wear resistance, high elastic limit, and low Young modulus [3]. However, the non-equilibrium processing techniques required to produce these alloys restrict their dimensions in the range of tens of millimeters, and severely limit their applications to small components and two-dimensional coatings [5].

There has been a number of attempts to fabricate MGs using laser processes [6–8]. In AM processes, because the interaction volume between the laser and the deposited powder is small, the interaction time is short, therefore, the local cooling rate is very high ( $10^3$ – $10^8$  K/s) [9], and typically higher than the critical cooling rate of most MGs [10]. In principle, coatings with an amorphous structure can, therefore, be produced by laser cladding. However, suppressing crystallization in the laser processing of MGs remains challenging because the heating rate

for avoiding crystallization is often higher than the heating rate actually achieved in the Heat-Affected Zone (HAZ). Zhu et al. [8] clad low carbon steel using a Fe-based metallic glass powder. They could achieve a partially amorphous coating. Lu et al. [11] used a Zr-based metallic glass powder to clad a steel substrate. Although they could not achieve a fully amorphous coating, corrosion resistance was improved compared to the unclad sample. Even small amounts of crystallization can be detrimental to the mechanical performance of the coating [12]. Although cladding of crystalline alloys with amorphous materials has been studied extensively, there are only a few studies focused on multi-layer cladding [13,14]. Yue et al. [14] clad a Mg-substrate via a Zr-based metallic glass. They used thick layers of pre-deposited powder with a high laser energy density to obtain full melting. This procedure led to a large HAZ. The authors commented on the thermal history in the HAZ of multi-layer laser processing, causing the formation of nanocrystals. Audebert et al. [13] used rescanning to reduce the effect of intermixing with the substrate, as the latter effect locally changes the chemical composition of the coating which is then more sensitive to crystallization. Hemmati et al. [15] investigated the effect of intermixing of Ni–Cr–B–Si–C on carbon steel. They found that reducing the energy density (reducing melt pool size) led to lower amount of intermixing. All the above studies show that optimizing parameters such as to provide both a good metallurgical bonding with the substrate and minimizing crystallization has always been a challenge [8,16].

In this study, for the first time, a Zr-based metallic glass (trade name AMZ4) is used for cladding. Thin layers of powder are used to minimize the required laser power, leading to small melt pool and HAZ, and

\* Corresponding author.

E-mail address: [navid.sohrabi@epfl.ch](mailto:navid.sohrabi@epfl.ch) (N. Sohrabi).<https://doi.org/10.1016/j.surfcoat.2020.126223>

Received 2 April 2020; Received in revised form 3 July 2020; Accepted 21 July 2020

Available online 23 July 2020

0257-8972/© 2020 The Authors. Published by Elsevier B.V. This is an open access article under the CC BY-NC-ND license

<http://creativecommons.org/licenses/by-nc-nd/4.0/>.

**Table 1**  
Chemical composition (wt%) of the Al-alloy substrate

Element	Al	Cu	Fe	Si	Pb	Bi	Others
wt%	Bal	5.0–6.0	0.0–0.7	0.0–0.4	0.2–0.4	0.2–0.6	0.0–0.4

reducing the effect of intermixing with the substrate. A new strategy is proposed for combining good bonding with the substrate and optimizing the coating properties, using two different sets of laser parameters, i.e. one for the first layer (interface between the coating and the substrate), and one for the rest of the coating. The first set of parameters is shown to ensure good bonding and absence of cracking at the interface, while the second set of parameters provides optimized density, hardness and wear resistance, and the lowest possible crystallinity.

## 2. Materials and methods

The powder used for cladding in this study was a gas atomized Zr-based MG powder (AMZ4) with a nominal composition of  $Zr_{59.3}Cu_{28.8}Al_{10.4}Nb_{1.5}$  (at.%) and particle size distribution ranging from 10  $\mu m$  to 50  $\mu m$  ( $D_{10} = 16 \mu m$ ,  $D_{50} = 30 \mu m$ , and  $D_{90} = 47 \mu m$ ), supplied by Heraeus Additive Manufacturing GmbH. The substrate was an AA2011-T6 aluminum alloy. The chemical composition of the substrate is given in Table 1.

The cladding process used a 500 W fiber laser, with a wavelength of 1070 nm and a spot size of 65  $\mu m$ . It was performed in an enclosed chamber pumping continuously the atmosphere while flowing nitrogen, such as to keep the oxygen level below 10 ppm. The laser scanning speed was kept constant (600 mm/s) and layer thicknesses (powder-bed depth) of 20 and 30  $\mu m$  were tested (16 and 11 cladded layers, respectively). Hatching distances from 50 to 110  $\mu m$  were used and the scanning strategy was parallel scanning with a change of 90° for each layer. The schematic of the cladding process is given in Fig. 1.

Vicker's microhardness measurements were performed using a Qness Q10A device on the cross-section of the coatings, according to ASTM E-384. All hardness tests were performed horizontally, except when the hardness evolution from the substrate to the coating was investigated (see Fig. 4c). The distance between two adjacent indents was at least three times the diameter of the indents. The samples were characterized by XRD (Panalytical Empyrean diffractometer) (Theta-Theta, 240 mm) in reflection mode and DSC (Netzsch DSC 204 F1 Phoenix at a heating rate of 20 °C/min). The XRD tests were performed

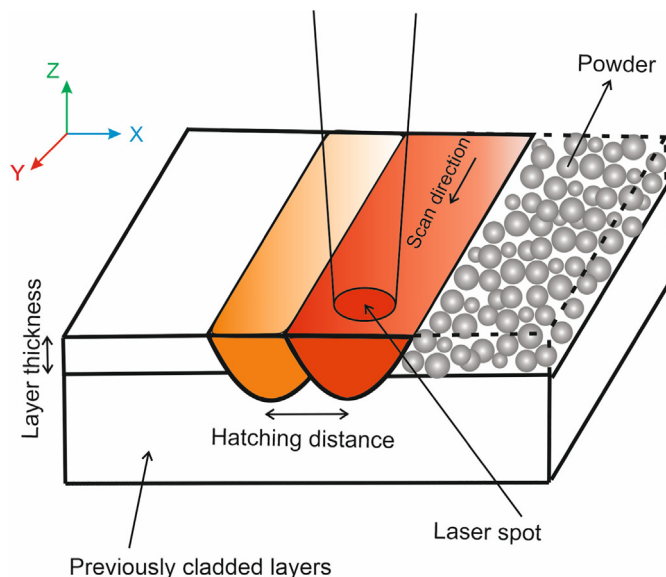


**Fig. 1.** Schematic of the cladding process performed in this study.

on the top surface (X-Y cross-section) after 100  $\mu m$  grinding. An FEI XLF30 field emission scanning electron microscope (FESEM) equipped with energy dispersive spectroscopy (EDS) and electron backscatter diffraction (EBSD) was used to detect the possible presence of crystals. The microstructure of the coating was revealed using an etching solution of 45 ml water + 45 ml  $HNO_3$  + 10 ml HF. The porosity content of the samples was determined by optical microscopy (OM) (Leica DM6000M) using the ImageJ® software.

Wear tests were carried out on the surface of the samples (polished down to sandpaper with 2500 mesh size) in a reciprocating tribometer with a ball-on-flat configuration. A more detailed description of the tribometer can be found in [17].  $Al_2O_3$  balls of 6 mm diameter were used as a counterpart. The applied normal force was 2 N at an average speed of 6 mm/s and 1 Hz frequency. The maximum contact pressure, shear stress, and the depth of maximum shear stress between the  $Al_2O_3$  ball and the coating were 685 MPa, 228 MPa, and 2  $\mu m$ , respectively, which was calculated using Hertz equation [18]. The duration of each test was 30 min, with a stroke length of 3 mm and a total sliding distance of 10.8 m. The sample surfaces and the counterpart balls were previously cleaned in ultrasound baths with acetone and subsequently in ethanol for 5 min each, and then dried with oil-free compressed air.

A 3D laser scanning confocal microscope, VK-X1000 Series, was used to measure the volume loss in each wear track. The average amount of volume loss of three wear tracks was reported.

## 3. Results and discussion

### 3.1. Optimization of processing parameters

An SEM image of the powder is shown in Fig. 2a. The spherical shape of the powder particles indicates that the powder flowability is likely to be suitable for powder-bed processing. The XRD pattern of the gas-atomized powder is represented in Fig. 2b. It shows a broad halo peak, which indicates that the powder is amorphous. Fig. 2c shows the DSC profile of the powder using the heating rate of 20 °C/min. The thermal information of the DSC test is presented in Table 2.

To study the effect of laser cladding parameters, samples were fabricated with a laser power varying from 80 W to 35 W with a decrement of 5 W, at a constant scanning speed, 600 mm/s. Two different layer thicknesses (20  $\mu m$  and 30  $\mu m$ ) were considered, and the hatching distance was varied from 50  $\mu m$  to 95  $\mu m$ . Fig. 3 illustrates the effect of laser power, layer thickness, and hatching distance on the Vicker's microhardness value of the coatings.

Fig. 3a indicates that the coating hardness drops with a decrease in the laser power, and saturates around 470 (HV2). The effect is illustrated with a 30  $\mu m$  layer thickness, but the trend is similar to a 20  $\mu m$  layer thickness. As the laser power (and energy density [19]) increases, both the melt pool and the HAZ become larger and promote crystallization [14,19]. Higher laser powers, therefore, led to higher hardness due to larger crystallized fraction.

Coatings fabricated with a laser power higher than 65 W exhibited cracks at the interface (see the inset of Fig. 3a). To have a good bonding between a coating and a substrate, a part of the substrate should be melted. Due to the Marangoni effect [16] and flow of the molten material in the melt pool, intermixing of the coating material and the substrate occurs. The mixing causes a change of local chemical composition and may introduce nucleation sites significantly affecting glass-forming ability (GFA). The process window preventing crystallization will, therefore, be reduced compared to that of the initial Zr-based MG. For example, the critical cooling rate will increase [20]. The effect of intermixing with the substrate affects only the first layers of the coating. High heating and cooling rates lead to significant thermal stresses, and at high laser power, crystallization will occur and increase the material brittleness. As crystallization is higher near the substrate, it leads to cracking at the interface.

Fig. 3b indicates that the coatings with 20  $\mu m$  layer thickness had a

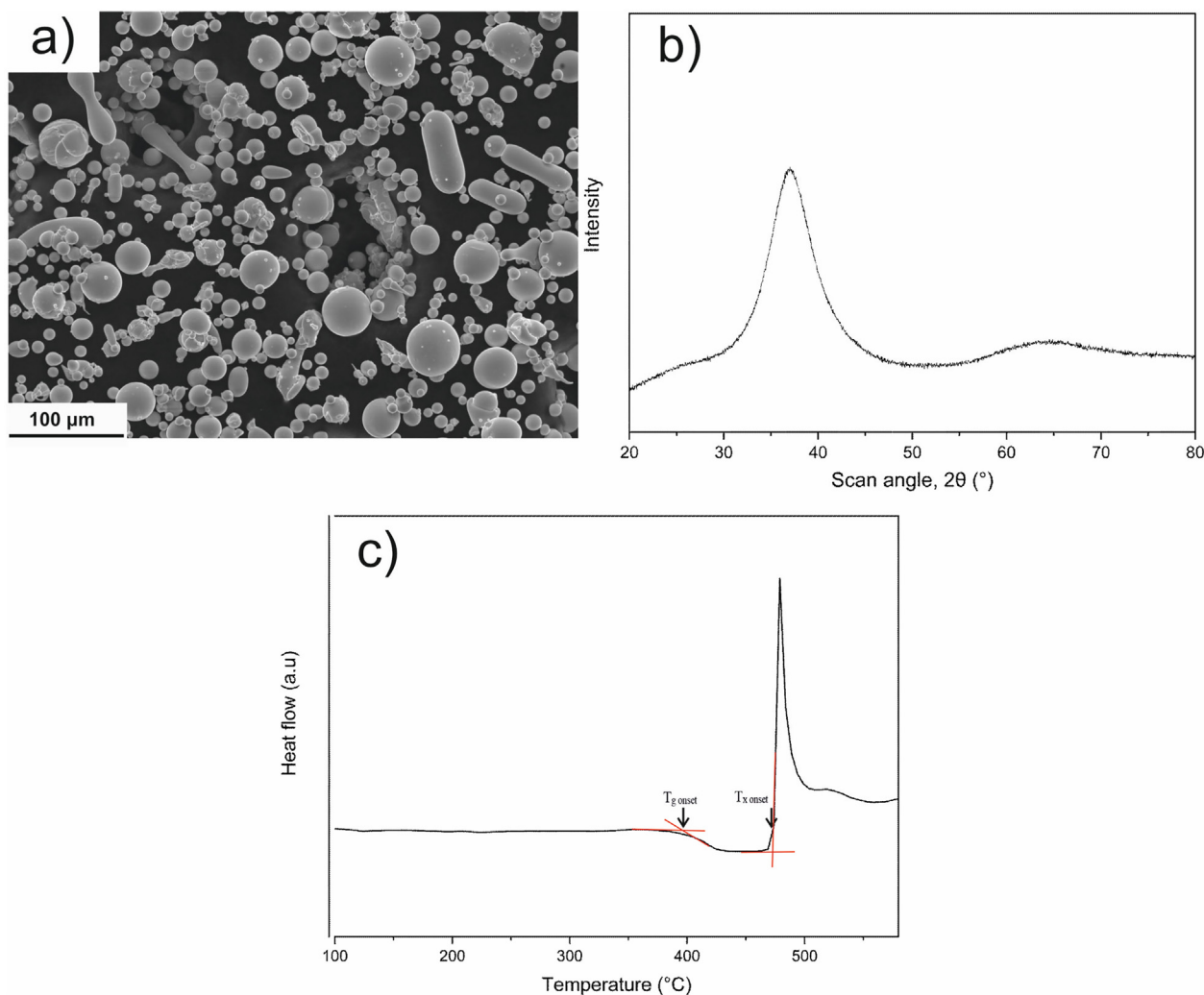


Fig. 2. a) SEM image of the gas atomized AMZ4 powder, b) XRD pattern of the powder, and c) DSC profile of the powder (heating rate of 20 °C/min).

higher hardness value compared to the coatings with 30  $\mu\text{m}$  layer thickness because of a higher energy density over the layer thickness, which led to a higher fraction of crystallization. Therefore, all remaining samples were produced with a layer thickness of 30  $\mu\text{m}$ . All obtained hardness values are higher than that of the amorphous material [21] ( $\text{HV}_2 = 450$ ), which means that all coatings were partially crystalline.

The hatching distance was varied from 50 to 95  $\mu\text{m}$  to increase the amorphous fraction of the coating (see Fig. 3c). For a given power, the hardness (and crystallized fraction) decreases with an increase of hatching distance. In the same way, for a given hatching distance, the coating manufactured with lower laser power exhibits a lower hardness (and crystallized fraction). Both effects come from a reduced energy density, which makes the Temperature-time (T-t) history less in favor of

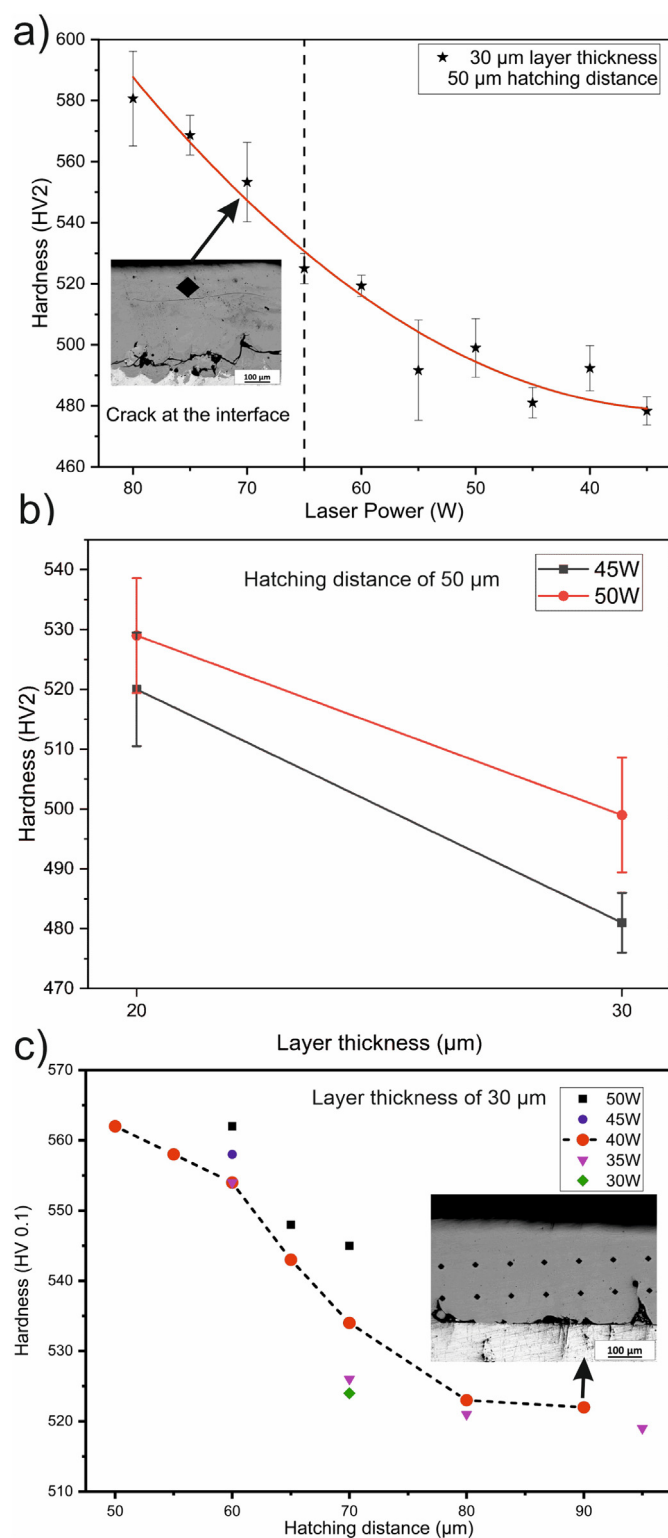
crystallization. However, a too low energy density leads to lack of fusion (LoF) defects. For instance, the coatings fabricated using a laser power less than 40 W and a hatching spacing larger than 70  $\mu\text{m}$  detached from the substrate because of the LoF porosity at the interface (see the inset of Fig. 3c). The coating exhibited a density below 99% which was mainly due to LoF.

Fig. 4a represents the XRD patterns of some of the coatings, indicating each time the laser power followed by the hatching distance, for a 30  $\mu\text{m}$  layer thickness. The samples produced with a higher power (40 W) display more peaks than the others. Their crystalline fraction is larger because of higher heat input. Since the increase in the hatching distance resulted in a global heat input decrease and reduced overlap between adjacent laser tracks, the trend was also a reduction of crystallinity. There is a broad pattern without any sharp diffraction peaks

**Table 2**  
Summary of the DSC results

Sample	$T_{g \text{ onset}}$ (°C)	$T_{x \text{ onset}}$ (°C)	$\Delta T$ (°C)	$\Delta H_x$ (J/g)	Amorphous <sup>a</sup> (%)
35 W-95 $\mu\text{m}$	397	472	75	100	99
35 W-80 $\mu\text{m}$	399	471	72	98	97
35 W-70 $\mu\text{m}$	395	472	77	92.6	92
40 W-90 $\mu\text{m}$	396	471	75	87.8	87
40 W-80 $\mu\text{m}$	396	471	75	84.8	84
AMZ4 powder	398	474	76	101	100

<sup>a</sup> Within the detection resolution of the DSC test.



**Fig. 3.** a) Effect of laser power on the hardness (HV2) values of the coating, at fixed layer thickness and hatching distance, b) effect of layer thickness on the hardness (HV2) values of the coating at fixed hatching distance, and c) effect of hatching distance on the hardness (HV 0.1) values of the coating, at fixed layer thickness.

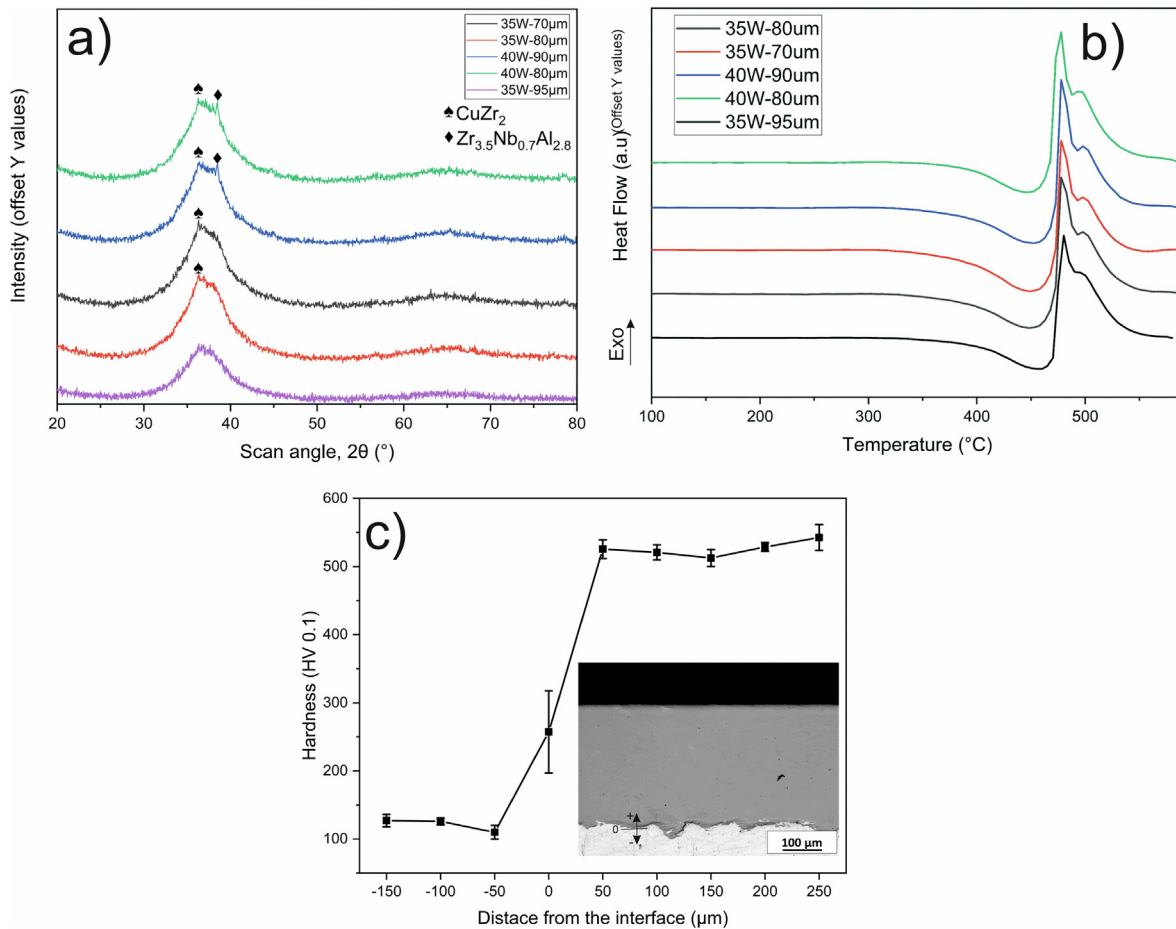
for the coating manufactured with 35 W-95  $\mu\text{m}$ , suggesting that the obtained coating is amorphous within the detection resolution of the XRD test.

Fig. 4b shows the DSC curves of the selected set of coatings and the

BMG powder. DSC results are representative of the mid-height region of the coating. The curves look identical, but their enthalpies of crystallization are different. The enthalpy of crystallization relates to the crystalline fraction in the coating [22]. The DSC curves of the coatings showed some asymmetry related to the overlap of two crystallization peaks. The observed behavior is due to a multi-step crystallization [23–28]. The amorphous phase transforms into one type of crystal and then that crystal to another type. K.M. Cole et al. [28] stated that the amorphous phase of their Zr-BMG first transforms into Cubic  $\text{Zr}_2\text{Ni}$  that, and then, into tetragonal  $\text{Zr}_2\text{Ni}$  and  $\text{Zr}_5\text{Ni}_4\text{Al}$ . Table 2 gives the onset temperature for glass transition,  $T_g$ , and crystallization of the first peak,  $T_x$ , the supercooled liquid region (SLR),  $\Delta T$ , and the enthalpy of crystallization,  $\Delta H_x$ , for several coatings. Compared to the powder sample, the onset temperatures for glass transition and crystallization of the coatings are shifted to lower temperatures, but generally, the corresponding SLR is slightly larger. The reduced glass transition ratio ( $T_g/T_1$ , melting point  $T_1 = 1188 \text{ K}$ ) is 0.56. Fu et al. [29] stated that a  $T_g/T_1$  higher than 0.6 indicates a good thermal stability and glass forming ability (GFA) of a metallic glass. In addition, A. Inoue [30] indicated that a wide SLR is an indication of a good GFA of the metallic glass. In the current study,  $T_g/T_1$  is slightly lower than the reported critical value, but a wide SLR (more than 70  $^\circ\text{C}$ ) compensates this limitation. It was assumed here that the powder was fully amorphous, and the amorphous fraction of each sample was calculated by dividing the crystallization enthalpy of the produced samples (measured by DSC) by the crystallization enthalpy of the powder. As crystallization increases hardness but reduces fracture toughness [31], the processing parameters leading to the highest amount of amorphous phase (according to the DSC tests), without any crystallization peak (according to the XRD tests), were selected, although other samples were crack free as well.

AM methods have the ability to vary the processing parameters between layers to decouple the properties at the interface and in the bulk. While a highly amorphous coating was obtained with 35 W-95  $\mu\text{m}$ , laser parameters have to be optimized to get an excellent bonding for the first layer at the interface with the substrate. To comply with two criteria of good bonding with the substrate (no LoF) and preventing cracking at the interface, a laser power of 60 W was selected. As shown in Fig. 3c, an increase in the hatching distance leads to lower hardness and consequently, higher amorphous content because of lower applied energy density. Therefore, the highest value of hatching distance (110  $\mu\text{m}$ ), which did not result in LoF at the interface with the substrate, was chosen. Thus, the first layer was clad with the laser power of 60 W, scanning speed of 600 mm/s, layer thickness of 30  $\mu\text{m}$  and hatching distance of 110  $\mu\text{m}$ . Compared to the inset of Fig. 3c (coatings without varying the laser power), coatings fabricated by varying the parameters from the interface to the bulk (see the inset of Fig. 4c) showed an excellent interface bonding without any cracks and LoF defects. The porosity content in the bulk of the coating was less than 0.5%. Fig. 4c shows the microhardness of the cross-section of the optimized coating. The sudden increase near the interface illustrates the high hardness of AMZ4 compared to the Al-substrate, with therefore expected improved surface properties.

Fig. 5a shows a coating cross-section SEM micrograph, in the optimized processing conditions. Using 60 W power for the first layer led to melting of the Al-substrate and made a good bonding between the coating and the substrate. To check the existence of micron and/or sub-micron size crystals in the coating, EBSD mapping with a step size of 200 nm was used. The band contrast map, which indicates all the diffracted phases, is presented in Fig. 5b. Through the bulk of the coating, no crystals were detected. The coating can be labeled amorphous in the sense that crystals larger than several hundreds of nanometer could not be detected (smaller nano-crystals can, however, exist). The larger grains at the bottom of the map are those of the Al-substrate, and the smaller ones are related to the MG partial crystallization in the first layer of the coating (with increased laser power). The elemental distribution across the interface (Fig. 5c) showed a uniform distribution of



**Fig. 4.** All the samples were printed with a layer thickness of 30  $\mu\text{m}$  with laser powers and hatching distances stated in the captions. a) XRD results of the coatings, b) DSC results of the coatings (heating rate of 20  $^{\circ}\text{C}/\text{min}$ ), and c) microhardness (HV 0.1) results of the coating produced by the optimized processing parameters (at the interface 60 W-110  $\mu\text{m}$  and for the bulk 35 W-95  $\mu\text{m}$ ). The inset is the OM micrograph of the coating cross-section with the processing parameters mentioned above.

the alloying elements in the coating, and mixing of alloy elements near the interface region, over a typical distance of 15–20  $\mu\text{m}$ , which is less than one layer thickness. The reason for a sudden increase of Al content and decrease in Zr, Cu, and Nb contents is the diffusion of a part of the Al-substrate in the intermixing region, which is indicated by a white arrow in Fig. 5a.

Fig. 6 shows SEM images from different regions of the coating after etching. The top part of the coating is presented in Fig. 6a. A part of melt pool 1 is remelted by melt pool 2 due to the overlap (hatching distance) between both tracks. Since this region is melted and solidified quickly, it is amorphous. There is a crystallized region on the left side of melt pool 2. This region was a part of the previous track (melt pool 1) and became HAZ of melt pool 2 (i.e., it was not remelted). Since this region experiences temperatures above the crystallization temperature of the material (and below the melting point), it is more susceptible to crystallization. The area fraction of crystals is, there, around  $3.7 \pm 0.6\%$ , using ImageJ<sup>®</sup>. However, this value may be slightly overestimated due to the etching procedure. A higher magnification image of region b is shown in Fig. 6b. Submicron crystals precipitated in the amorphous matrix are detected in the HAZ. The average size of the nano-crystals is  $233 \pm 93$  nm. EBSD measurements could therefore not detect these nano-crystals, considering the 200 nm step size (a few pixels are needed).

Fig. 6c shows an SEM image at the mid-height of the coating. The area fraction of crystals in this area was increased to  $5.7 \pm 0.8\%$ , due to thermal effects introduced by the subsequently added layers. The reason for the discrepancy between the crystallization fraction measured by DSC (1%) and SEM images is that DSC analysis is not sensitive

enough to detect localized nano-crystallization. According to Allen et al. [32], the heat generation of nano-crystals is extremely weak, and cannot be measured accurately with conventional DSC systems. Likewise, XRD tests did not show any crystalline peak for the optimized sample, indicating that the fraction of nano-crystals was below the detection limit. In small amounts, however, the presence of nanocrystals does not change dramatically most of the mechanical properties [33]; it is, therefore, acceptable to rely on the (quasi) absence of crystallization from standard DSC or XRD measurements, when these mechanical properties are of concern. The interface of the coating and the substrate is finally presented in Fig. 6d. It clearly depicts the intermixing region and the related occurrence of crystallization. The rectangular region e in Fig. 6d is rotated by 90 $^{\circ}$  (counter-clockwise) and shown with higher magnification in Fig. 6e. An EDS line scan was carried out along the yellow line to check the distribution of elements in the intermixing region. It can be seen in Fig. 6f that oscillations of Zr, Al, and Nb content are often correlated, as one would expect from the chemical composition of the alloy. At one location (at the distance of 15  $\mu\text{m}$ ), only the amount of Al has increased, which can be attributed to the diffusion from the substrate. According to Shen et al. [34], BMGs are very sensitive to the change in the chemical composition of elements, and this change can strongly influence their crystallization behavior. We, therefore, assume these chemical effects promote crystallization near the interface with the substrate.

### 3.2. Wear behavior

Fig. 7a–d show confocal microscopy images of wear tracks and

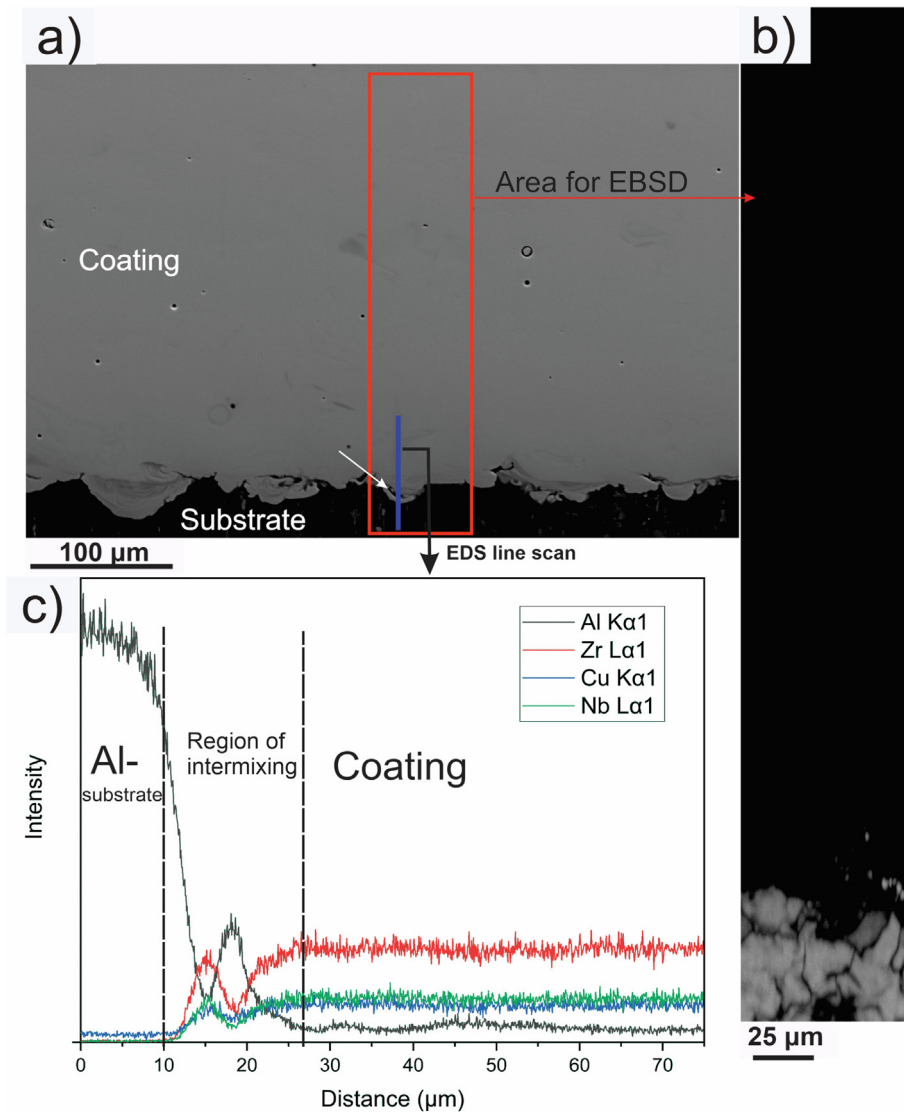


Fig. 5. a) SEM micrograph of the cross-section of the optimized coating (the power and the hatching distance used for the first layer above the interface were 60 W and 110 μm, (60 W-110 μm), respectively and for the bulk 35 W-95 μm), b) EBSD band contrast of the area marked in (a), and c) EDS line scan across the interface showing the evolution of chemistry.

Fig. 7e presents the volume loss in the wear tests. It indicates a significant increase in wear resistance when the substrate is clad with Zr-based metallic glass. The inset of Fig. 7e highlights the differences associated with different cladding parameters. As the crystallization fraction increases, the volume loss decreases, which is consistent with the higher hardness of the crystalline phase compared to the amorphous phase. These results are consistent with the finding of H.W et al. [6] for laser cladding of titanium with a Ti-based metallic glass. Yue et al. [14] used a Zr-metallic glass for cladding a magnesium substrate and also observed that the increase in hardness resulted in higher wear resistance. In addition, they indicated that samples containing nanocrystals had better wear resistance than amorphous samples, but reduced corrosion resistance.

The compressive yield strength of AMZ4 is 1.4 GPa [33], which is higher than the applied maximum contact pressure. As mentioned earlier, the maximum depth of the shear stress was 2 μm and the depth of the wear track in Fig. 7d is 9 μm. These two values are much lower than the thickness of the coating, which is 300 μm. Therefore, the substrate is not affected by the wear of the coating.

Cardinal et al. [31] investigated the effect of crystallization on the toughness of a gold-based BMG. They observed that crystallization

caused brittleness, the toughness decreasing as the crystalline fraction increased. Ketkaew et al. [35] studied the crystallization of Zr-based and Pd-based BMGs. Crystallization up to 6% in volume did not affect the fracture toughness, but one additional percent of crystallization decreased it by 50%. In the current study, although higher crystalline fractions lead to better wear resistance, the total fraction must remain as low as possible such as to provide reasonable toughness, and prevent cracking during processing. Indeed, cladding operating at high powers, such as the cladding fabricated by the power of 70 W, layer thickness of 30 μm, hatching distance of 50 μm and scanning speed of 600 mm/s, did lead to cracks in the coating (see the inset of Fig. 3a). Since the wear resistance of the sample with 16% crystallization (40 W-80 μm) was not even twice that of the sample with 1% crystallization (35 W-95 μm), and because we did not want to jeopardize the toughness of the coating, the condition with 35 W-95 μm was considered as the optimal one. The wear-rate of the coating fabricated with the optimal parameters is  $1.44 \times 10^{-4} \text{ mm}^3 \cdot \text{N}^{-1} \cdot \text{m}^{-1}$ .

Since the chosen wear testing conditions such as substrates, coating, applied force, sliding speed and distance are different from other literature results, a comparison of the ratio of the wear rates of Aluminum alloys substrates to the wear rates of different coatings is presented in

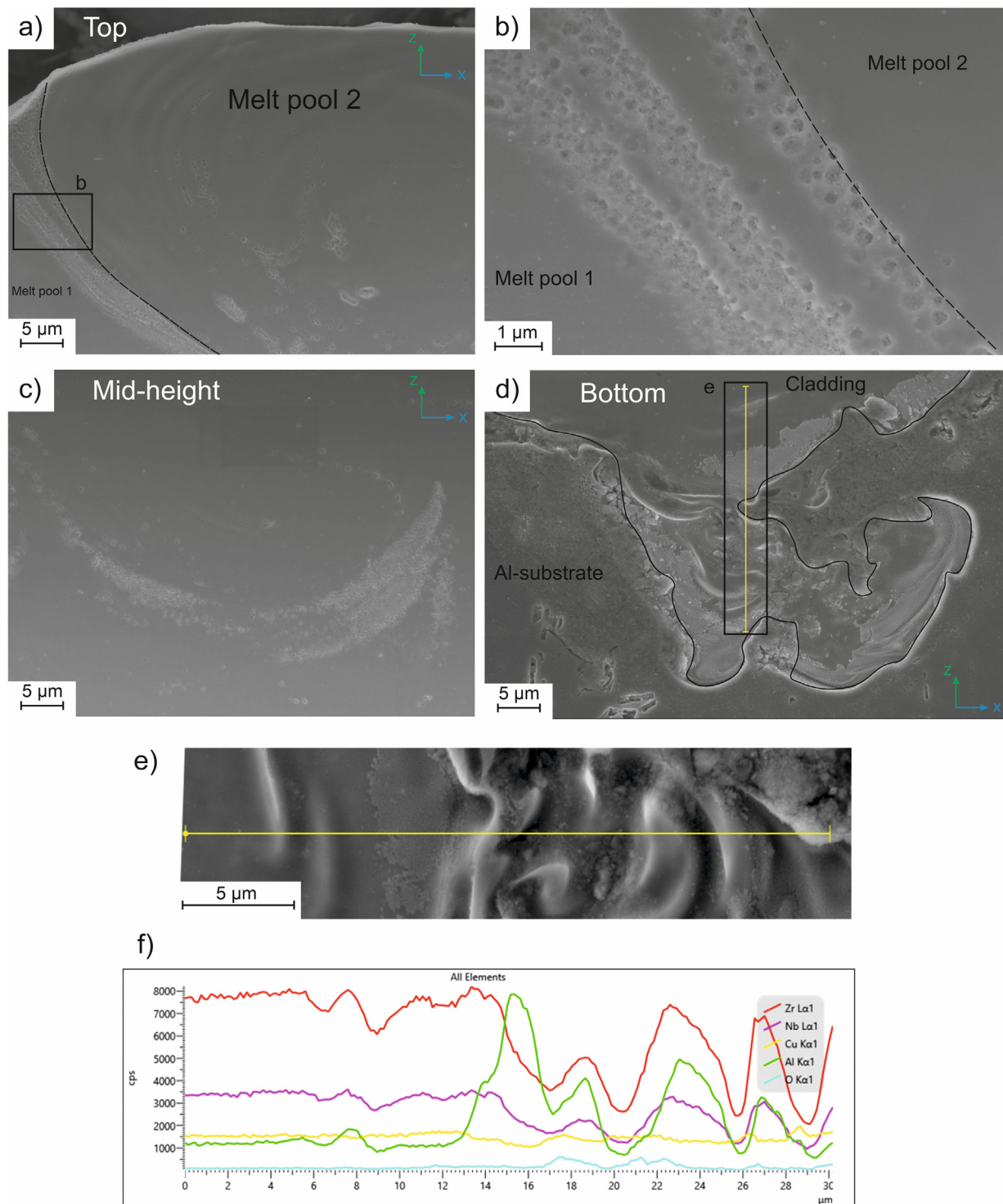


**Fig. 6.** SEM images of different regions of the coating, a) top part, b) magnified region b found in a), c) mid-height part, d) bottom part of the coating where intermixing occurs, e) magnified region e (rotated 90° counter-clockwise) found in d) where EDS line (along the yellow line) analysis was carried out, and f) EDS spectra of the yellow line in f). (For interpretation of the references to color in this figure legend, the reader is referred to the web version of this article.)

**Fig. 8.** This ratio was defined as relative wear resistance by Wong et al. [36]. When using this representation, the proposed AMZ4 coating shows excellent performance, even though the average hardness of our aluminum substrate at 5 kg (HV5), 300 g (HV0.3), and 50 g (HV0.05) force is  $120.2 \pm 4$ ,  $132.4 \pm 7.2$ , and  $125.4 \pm 11.1$ , respectively, i.e. higher than the substrate hardness values reported in the other studies: 80 (HV5) [37], 110 (HV0.05) [36], and 60 (HV0.3) [38].

Fig. 9a shows an SEM image of the wear track of the sample printed

with the optimized parameters (Fig. 7d), which led to 1% crystallization. Regions b and c are zoomed in Fig. 9b and c. Wear debris are shown at Point 1 and Point 3, while zones such as Point 2 and Point 4 correspond to the undamaged coating. EDS analyses were performed at Points 1 to 4, and the results are presented in Table 3. Points 1 and 3 indicate the presence of oxygen, while Points 2 and 4 do not show unexpected composition. The oxygen content is attributed to the reaction of wear debris with oxygen in the air, probably resulting in

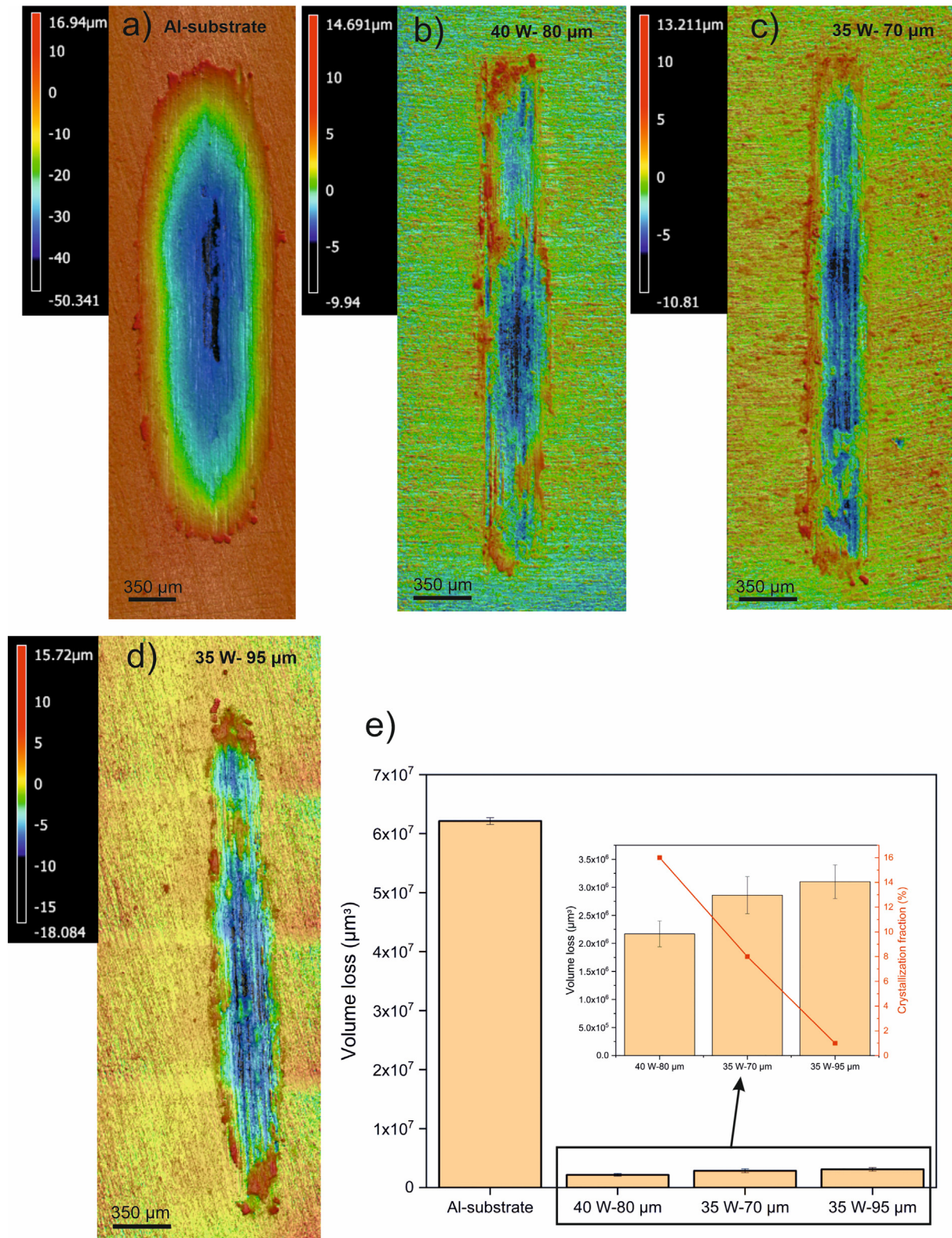


Fig. 7. Confocal microscopy image of a wear track on Al-substrate (a), and cladded samples with: b) the power of 40 W and hatching distance of 80  $\mu\text{m}$ , c) the power of 35 W and hatching distance of 70  $\mu\text{m}$ , d) the power of 35 W and hatching distance of 95  $\mu\text{m}$ , the color bar of the legends corresponds to the distance from the original surface before the wear tests e) wear test quantitative results with inset zooming on the volume loss changes for different cladding parameters.

oxidized Zr [22]. Based on the morphologies of the wear track and debris, the wear mechanism was a combination of abrasive-wear and oxidation-wear, which is consistent with the study of Zhang et al. [39]

#### 4. Conclusion

In this study, multi-layers of a Zr-based metallic glass were cladded on an aluminum alloy via laser additive manufacturing. The

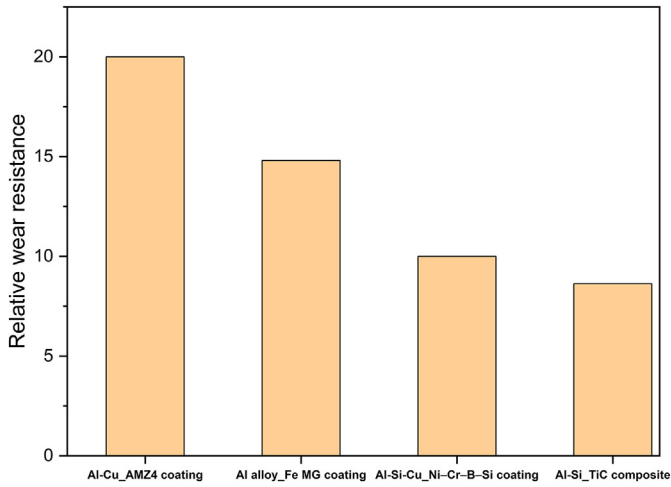


Fig. 8. Comparison of relative wear resistance (ratio of substrate wear rate to coating wear rate) of AMZ4 (Zr-based MG), Fe-based MG [38], Ni-Cr-B-Si [36] coatings and TiC composite [37] on aluminum alloy substrates.

Table 3

Element composition (wt%) of the four points shown in Fig. 9b and c measured by EDS working at 20 kV

Location	Element composition (wt%)				
	Zr	Cu	Al	Nb	O
Point 1	66.3	19.2	3.9	5.3	8.3
Point 2	67.6	23.1	3.4	6	–
Point 3	56.2	19.6	2.9	5.3	15.9
Point 4	67.2	23.4	3.4	6	–

microstructure and mechanical properties of the coating were studied, and the following results can be outlined:

- 1) AMZ4 MG powder was successfully cladded on an aluminum substrate to a thickness of 300 μm with less than 0.5% porosity content and the laser power threshold for crack initiation at the interface was identified.
- 2) To obtain an excellent crack-free coating, two different sets of laser parameters were used, near the interface and in the bulk. The energy density of the first layer was higher in order to melt the powder and

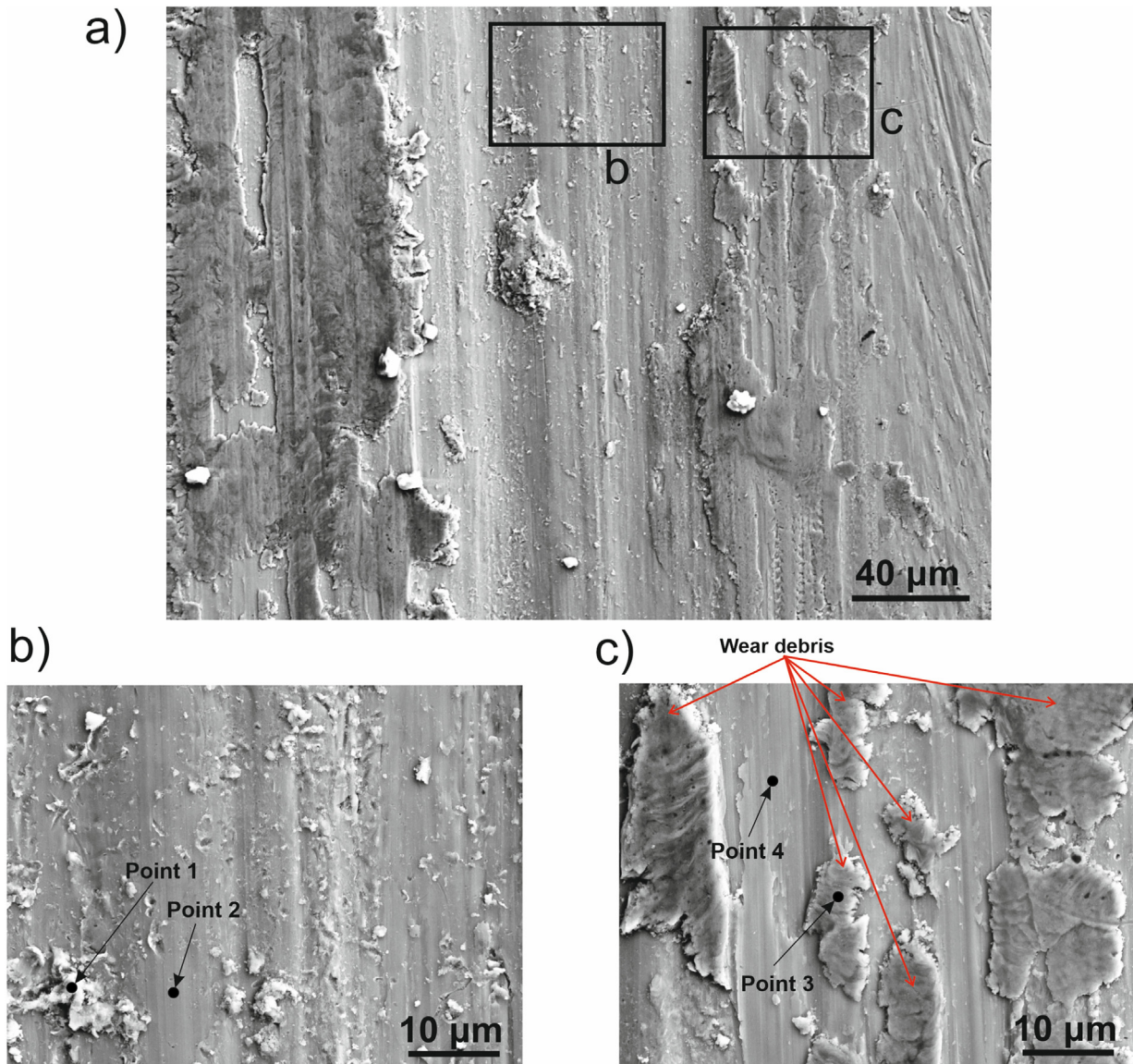


Fig. 9. a) SEM micrograph of the wear track shown in Fig. 7d (35 W-95 μm), b) magnified image of region b in (a), and c) magnified image of region c in (a).

the solid substrate, and led to good bonding at the interface. Laser parameters leading to a lower energy density were used in the bulk of the coating, achieving a density higher than 99.5%, and maximizing the amorphous fraction.

- A higher crystalline fraction leads to a harder coating, and a lower wear rate. However, the toughness needs to be considered as crystallization leads to brittleness and cracking. As a consequence, the lowest crystalline fraction represents the optimum condition. The hardness of the coating is quasi-uniform throughout the thickness.
- The presence of nano-crystals was beyond the detection limit of XRD, DSC, and EBSD measurements (using a step size of 200 nm). Nano-crystals were identified from SEM images (average size of 233 nm) and result in a crystallized fraction between 4 and 6% in the optimized sample.
- Two mechanisms of crystallization operated in the coating. One was related to the change of chemical composition near the substrate (confirmed by EDS), and the other resulted from the thermal history in the Heat-Affected Zones (HAZs) of the laser tracks.
- The wear resistance of the amorphous coating was 20 times higher than that of the substrate, which places it among the best possible coatings for Aluminum alloys.

In conclusion, this study demonstrates that multi-layer cladding of a Zr-based metallic glass on aluminum parts is possible, and highly beneficial for applications where mechanical properties such as wear-resistance and hardness are crucial.

#### CRedit authorship contribution statement

**Navid Sohrabi:** Conceptualization, Methodology, Validation, Formal analysis, Investigation, Writing - original draft, Visualization. **Ramanandan Santhanu Panikar:** Methodology, Validation, Formal analysis, Investigation, Writing - original draft, Visualization. **Jamasp Jhabvala:** Conceptualization, Writing - review & editing, Supervision. **Alejandro Roda Buch:** Resources, Methodology, Formal analysis, Writing - review & editing. **Stefano Mischler:** Resources, Writing - review & editing. **Roland E. Logé:** Conceptualization, Resources, Project administration, Funding acquisition, Writing - review & editing, Supervision.

#### Declaration of competing interest

The authors declare that they have no known competing financial interests or personal relationships that could have appeared to influence the work reported in this paper.

#### Acknowledgment

This work was supported by the "PRECision Additive Manufacturing of Precious metals Alloys (PREAMPA)" project. The PREAMPA project is funded by the Swiss ETH domain, Switzerland domain, within the Strategic Focus Area on Advanced Manufacturing. The generous support of PX Group to the LMTM laboratory is also highly acknowledged.

#### References

- A.P.I. Popoola, O.S. Fatoba, H.W. Nkosi, V.S. Aigbodion, Surface hardening of aluminum by laser alloying with molybdenum and zirconium powder, *Int. J. Electrochem. Sci.* 11 (2016) 126–139.
- A. Krzymień, P. Krzymień, Application of aluminum alloys for combustion engine bearings, *J. KONES* 14 (2007) 233–238.
- J. Schroers, G. Kumar, T.M. Hodges, S. Chan, T.R. Kyriakides, Bulk metallic glasses for biomedical applications, *JOM* 61 (2009) 21–29, <https://doi.org/10.1007/s11837-009-0128-1>.
- E. Williams, N. Lavery, Laser processing of bulk metallic glass: a review, *J. Mater. Process. Technol.* 247 (2017) 73–91, <https://doi.org/10.1016/j.jmatprotec.2017.03.034>.
- S. Pauly, L. Löber, R. Petters, M. Stoica, S. Scudino, U. Kühn, J. Eckert, Processing Metallic Glasses by Selective Laser Melting, (2013), <https://doi.org/10.1016/j.matmod.2013.01.018>.
- H. Wu, L. Liang, X. Lan, Y. Yin, M. Song, R. Li, Y. Liu, H. Yang, L. Liu, A. Cai, Q. Li, W. Huang, Tribological and biological behaviors of laser clad Ti-based metallic glass composite coatings, *Appl. Surf. Sci.* 507 (2020) 145104, <https://doi.org/10.1016/j.apsusc.2019.145104>.
- X. Ye, Y.C. Shin, Synthesis and characterization of Fe-based amorphous composite by laser direct deposition, *Surf. Coat. Technol.* 239 (2014) 34–40, <https://doi.org/10.1016/j.surfcoat.2013.11.013>.
- Y.Y. Zhu, Z.G. Li, R.F. Li, M. Li, X.L. Daze, K. Feng, Y.X. Wu, Microstructure and property of Fe-Co-B-Si-C-Nb amorphous composite coating fabricated by laser cladding process, *Appl. Surf. Sci.* 280 (2013) 50–54, <https://doi.org/10.1016/j.apsusc.2013.04.077>.
- T. DebRoy, H.L. Wei, J.S. Zuback, T. Mukherjee, J.W. Elmer, J.O. Milewski, A.M. Beese, A. Wilson-Heid, A. De, W. Zhang, Additive manufacturing of metallic components – process, structure and properties, *Prog. Mater. Sci.* 92 (2018) 112–224, <https://doi.org/10.1016/j.pmatsci.2017.10.001>.
- J. Heinrich, R. Busch, B. Nonnenmacher, Processing of a bulk metallic glass forming alloy based on industrial grade Zr, *Intermetallics* 25 (2012) 1–4, <https://doi.org/10.1016/j.intermet.2012.02.011>.
- Y. Lu, H. Li, H. Zhang, G. Huang, H. Xu, Z. Qin, X. Lu, Zr-based metallic glass coating for corrosion resistance improvement of 45 steel, *Mater. Trans.* 58 (2017) 1319–1321, <https://doi.org/10.2320/matertrans.M2017118>.
- J. Schroers, Processing of bulk metallic glass, *Adv. Mater.* 22 (2010) 1566–1597, <https://doi.org/10.1002/adma.200902776>.
- F. Audebert, R. Colaço, R. Vilar, H. Sirkin, Production of glassy metallic layers by laser surface treatment, *Scr. Mater.* 48 (2003) 281–286, [https://doi.org/10.1016/S1359-6462\(02\)00382-2](https://doi.org/10.1016/S1359-6462(02)00382-2).
- T.M. Yue, Y.P. Su, Laser multi-layer cladding of Zr65Al7.5Ni10Cu17.5 amorphous alloy on magnesium substrates, *J. Mater. Sci.* 42 (2007) 6153–6160, <https://doi.org/10.1007/s10853-006-1134-0>.
- I. Hemmati, V. Ocelik, J.T.M. De Hosson, Dilution effects in laser cladding of Ni-Cr-B-Si-C hardfacing alloys, *Mater. Lett.* 84 (2012) 69–72, <https://doi.org/10.1016/j.matlet.2012.06.054>.
- Y. Lu, G. Huang, Y. Wang, H. Li, Z. Qin, X. Lu, Crack-free Fe-based amorphous coating synthesized by laser cladding, *Mater. Lett.* 210 (2018) 46–50, <https://doi.org/10.1016/j.matlet.2017.08.125>.
- J. Stojadinovic, D. Bouvet, M. Declercq, S. Mischler, Influence of chelating agents on the tribocorrosion of tungsten in sulphuric acid solution, *Electrochim. Acta* 56 (2011) 7131–7140, <https://doi.org/10.1016/j.electacta.2011.05.084>.
- K.L. Johnson, *Contact Mechanics*, Cambridge University Press, 1985, <https://doi.org/10.1201/b17110-2>.
- X.P. Li, M.P. Roberts, S. O'Keeffe, T.B. Sercombe, Selective laser melting of Zr-based bulk metallic glasses: processing, microstructure and mechanical properties, *Mater. Des.* 112 (2016) 217–226, <https://doi.org/10.1016/j.matdes.2016.09.071>.
- A. Basu, A.N. Samant, S.P. Harimkar, J.D. Majumdar, I. Manna, N.B. Dahotre, Laser surface coating of Fe-Cr-Mo-Y-B-C bulk metallic glass composition on AISI 4140 steel, *Surf. Coat. Technol.* 202 (2008) 2623–2631, <https://doi.org/10.1016/j.surfcoat.2007.09.028>.
- P. Bordeenthikasem, M. Stolpe, A. Elsen, D.C. Hofmann, Glass forming ability, flexural strength, and wear properties of additively manufactured Zr-based bulk metallic glasses produced through laser powder bed fusion, *Addit. Manuf.* 21 (2018) 312–317, <https://doi.org/10.1016/j.addma.2018.03.023>.
- H.W. Jin, R. Ayer, J.Y. Koo, R. Raghavan, U. Ramamurty, Reciprocating wear mechanisms in a Zr-based bulk metallic glass, *J. Mater. Res.* 22 (2007) 264–273, <https://doi.org/10.1557/jmr.2007.0048>.
- D. Ouyang, N. Li, L. Liu, Structural heterogeneity in 3D printed Zr-based bulk metallic glass by selective laser melting, *J. Alloys Compd.* 740 (2018) 603–609, <https://doi.org/10.1016/j.jallcom.2018.01.037>.
- W.L.J.R. Busch, S. Schneider, A. Peker, Decomposition and primary crystallization in undercooled Zr41.2Ti13.8Cu12.5Ni10.0Be22.5 melts, *Appl. Phys. Lett.* 67 (1995) 1544–1546, <https://doi.org/10.1063/1.114487>.
- W.L.J.S. Schneider, P. Thiyagarajan, Formation of nanocrystals based on decomposition in the amorphous Zr41.2Ti13.8Cu12.5Ni10.0Be22.5 alloy, *Appl. Phys. Lett.* 68 (1996) 493–495.
- A.A. Kündig, J.F. Löffler, W.L. Johnson, P.J. Uggowitzer, P. Thiyagarajan, Influence of decomposition on the thermal stability of undercooled Zr-Ti-Cu-Ni-Al alloys, *Scr. Mater.* 44 (2001) 1269–1273, [https://doi.org/10.1016/S1359-6462\(01\)00691-1](https://doi.org/10.1016/S1359-6462(01)00691-1).
- Y.H. Li, W. Zhang, C. Dong, J.B. Qiang, A. Makino, Correlation between the glass-forming ability and activation energy of crystallization for Zr75-xNi25Al x metallic glasses, *Int. J. Miner. Metall. Mater.* 20 (2013) 445–449, <https://doi.org/10.1007/s12613-013-0749-9>.
- K.M. Cole, D.W. Kirk, C.V. Singh, S.J. Thorpe, Role of niobium and oxygen concentration on glass forming ability and crystallization behavior of Zr-Ni-Al-Cu-Nb bulk metallic glasses with low copper concentration, *J. Non-Cryst. Solids* 445–446 (2016) 88–94, <https://doi.org/10.1016/j.jnoncrysol.2016.05.015>.
- Y. Fu, B. Shen, H. Kimura, A. Makino, A. Inoue, Enhanced glass-forming ability of FeCoBSiNb bulk glassy alloys prepared using commercial raw materials through the optimization of Nb content, *J. Appl. Phys.* 107 (2010) 1–4, <https://doi.org/10.1063/1.3350898>.
- A. Inoue, High strength bulk amorphous alloys with low critical cooling rates, *Mater. Trans.* 36 (1995) 866–875, <https://doi.org/10.2320/matertrans1989.36.866>.
- S. Cardinal, J.M. Pelletier, M. Eisenbart, U.E. Klotz, Influence of crystallinity on thermo-process ability and mechanical properties in a Au-based bulk metallic glass, *Mater. Sci. Eng. A* 660 (2016) 158–165, <https://doi.org/10.1016/j.msea.2016.02>.

- 078.
- [32] D.R. Allen, J.C. Foley, J.H. Perepezko, Nanocrystal development during primary crystallization of amorphous alloys, *Acta Mater.* 46 (1998) 431–440, [https://doi.org/10.1016/S1359-6454\(97\)00279-6](https://doi.org/10.1016/S1359-6454(97)00279-6).
- [33] N. Sohrabi, J. Jhabvala, G. Kurtuldu, M. Stoica, A. Parrilli, S. Berns, S. Hugon, A. Neels, J.F. Löffler, R.E. Logé, Characterization, Mechanical Properties, and Dimensional Accuracy of a Zr-based Bulk Metallic Glass Manufactured Via Laser Powder-bed Fusion. (n.d.) (Under Prep).
- [34] Y. Shen, Y. Li, C. Chen, H.L. Tsai, 3D printing of large, complex metallic glass structures, *Mater. Des.* 117 (2017) 213–222, <https://doi.org/10.1016/j.matdes.2016.12.087>.
- [35] J. Ketkaew, Z. Liu, W. Chen, J. Schroers, Critical crystallization for embrittlement in metallic glasses, *Phys. Rev. Lett.* 265502 (2015) 1–6, <https://doi.org/10.1103/PhysRevLett.115.265502>.
- [36] T.T. Wong, G.Y. Liang, B.L. He, C.H. Woo, Wear resistance of laser-clad Ni-Cr-B-Si alloy on aluminium alloy, *J. Mater. Process. Technol.* 100 (2000) 142–146, [https://doi.org/10.1016/S0924-0136\(99\)00463-X](https://doi.org/10.1016/S0924-0136(99)00463-X).
- [37] L. Dubourg, D. Ursescu, F. Hlawka, A. Cornet, Laser cladding of MMC coatings on aluminium substrate: influence of composition and microstructure on mechanical properties, *Wear* 258 (2005) 1745–1754, <https://doi.org/10.1016/j.wear.2004.12.010>.
- [38] A. Singh, S.R. Bakshi, A. Agarwal, S.P. Harimkar, Microstructure and tribological behavior of spark plasma sintered iron-based amorphous coatings, *Mater. Sci. Eng. A* 527 (2010) 5000–5007, <https://doi.org/10.1016/j.msea.2010.04.066>.
- [39] J.J. Marattukalam, V. Pacheco, D. Karlsson, L. Riekehr, J. Lindwall, F. Forsberg, U. Jansson, M. Sahlberg, B. Hjärvarsson, Development of process parameters for selective laser melting of a Zr-based bulk metallic glass, *Addit. Manuf.* 33 (2020) 101124, <https://doi.org/10.1016/j.addma.2020.101124>.